

# Hallmark of quantum skipping in energy filtered lensless scanning electron microscopy

Cite as: Appl. Phys. Lett. **120**, 052403 (2022); doi: [10.1063/5.0077503](https://doi.org/10.1063/5.0077503)

Submitted: 3 November 2021 · Accepted: 19 January 2022 ·

Published Online: 2 February 2022



View Online



Export Citation



CrossMark

A.-K. Thamm,<sup>1</sup> J. Wei,<sup>1</sup>  J. Zhou,<sup>1,a)</sup> C. G. H. Walker,<sup>1</sup> H. Cabrera,<sup>1</sup> M. Demydenko,<sup>1</sup> D. Pescia,<sup>1,b)</sup>  U. Ramsperger,<sup>1</sup> A. Suri,<sup>2</sup> A. Pratt,<sup>3</sup> S. P. Tear,<sup>3</sup>  and M. M. El-Gomati<sup>3,4</sup>

## AFFILIATIONS

<sup>1</sup>Laboratory for Solid State Physics, ETH Zurich, 8093 Zurich, Switzerland

<sup>2</sup>Corelab for Correlative Microscopy and Spectroscopy, Helmholtz-Zentrum Berlin, Hahn-Meitner-Platz 1, 14109 Berlin, Germany

<sup>3</sup>Department of Physics, University of York, Heslington, York YO10 5DD, United Kingdom

<sup>4</sup>York Probe Sources Ltd, 7 Harwood Rd., York YO26 6QU, United Kingdom

<sup>a)</sup>Present address: Laboratory for Mesoscopic Systems, Department of Materials, ETH Zurich, 8093 Zurich, Switzerland and Laboratory for Multiscale Materials Experiments, Paul Scherrer Institute, 5232 Villigen PSI, Switzerland.

<sup>b)</sup>Author to whom correspondence should be addressed: [pescia@solid.phys.ethz.ch](mailto:pescia@solid.phys.ethz.ch)

## ABSTRACT

We simulate the electronic system of ejected electrons arising when a tip, positioned few 10 nm away from a surface, is operated in the field emission regime. We find that, by repeated quantum reflections (“quantum skipping”), electrons produced at the nanoscale primary site are able to reach the macroscopic environment surrounding the tip-surface region. We observe the hallmark of quantum skipping in an energy filtered experiment that detects the spin of the ejected electrons.

© 2022 Author(s). All article content, except where otherwise noted, is licensed under a Creative Commons Attribution (CC BY) license (<http://creativecommons.org/licenses/by/4.0/>). <https://doi.org/10.1063/5.0077503>

Like tunneling, reflection at an energy cliff is a purely quantum mechanical phenomenon.<sup>1</sup> It has been observed, e.g., for electrons,<sup>2–6</sup> neutrons,<sup>7</sup> and atoms,<sup>8,9</sup> and also has practical applications, e.g., in devices involving electron emission and injection.<sup>10,11</sup> Here, we show that a special situation of scanning electron microscopy, where the electron source is only a few nanometers away from the target,<sup>12–15</sup> is unique in that quantum skipping (i.e., repeated quantum reflections) is the only mechanism that allows electrons produced at the primary, nanoscale site,<sup>14</sup> to reach the macroscopic environment. Our simulations show that the ejected electrons, skipping away from the primary site, accumulate in the elastic channel. Accordingly, energy filtered experiments, detecting the spin of the ejected electrons as a marker, find precisely in the elastic peak the sought-after nanoscale locality. Because of these observations, a technology that integrates, in one instrument, low energy lensless scanning electron microscopy<sup>16–21</sup> with tunneling-based scanning probe methods<sup>22</sup> and, as such, is distinct from other tools used, e.g., in magnetic imaging (see, e.g., Ref. 23 for a brief summary of magnetic imaging methods), finds a solid foundation.

In the first part of this paper, we explore, numerically, the properties of the ejected electron system. (Detail of the simulations is given in

the [supplementary material](#).) The ejected electrons represent an electronic system, which is not present when the tip is in the scanning tunneling microscopy regime.<sup>22</sup> We make no attempt at describing the field emission process: The model simulations start with low energy electrons traveling along the tip axis and arriving at the primary site with some kinetic energy. Once arrived, the electrons are either reflected back along the tip axis (in which case they are removed from the simulation) by quantum reflection or they are allowed to enter the target and scatter elastically and inelastically with its constituents. The scattering processes within the target at the primary site and at the reentrance sites are handled by the Geant4 software<sup>24,25</sup> ([supplementary material](#)). The scattering events at the primary site establish a reservoir of backscattered electrons with a certain angular distribution around the normal. Those electrons that emerge into the vacuum after scattering are transferred to the COMSOL-Multiphysics software<sup>26</sup> to be propagated along the vacuum side of the surface ([supplementary material](#)). Some of them may reflect at the surface cliff (and may do so several times), producing a system of skipping electrons propagating almost parallel to the surface. (Until, at micrometer distances from the tip-vacuum-sample junction, they get attracted away by the detector.) If not reflected at the surface, they reenter the material and are handed

back to the Geant4 software. In Fig. 1(a), we show simulated<sup>26</sup> trajectories of elastic and inelastic ejected electrons emerging at the primary site at energies of a few tens of eV, typical for the voltages at which the tip-vacuum-sample junction is operated.<sup>14</sup> The ejected electrons are, without exception, bent toward the surface by the strong electric field that is used to field-emit the electrons from the tip. Upon landing back

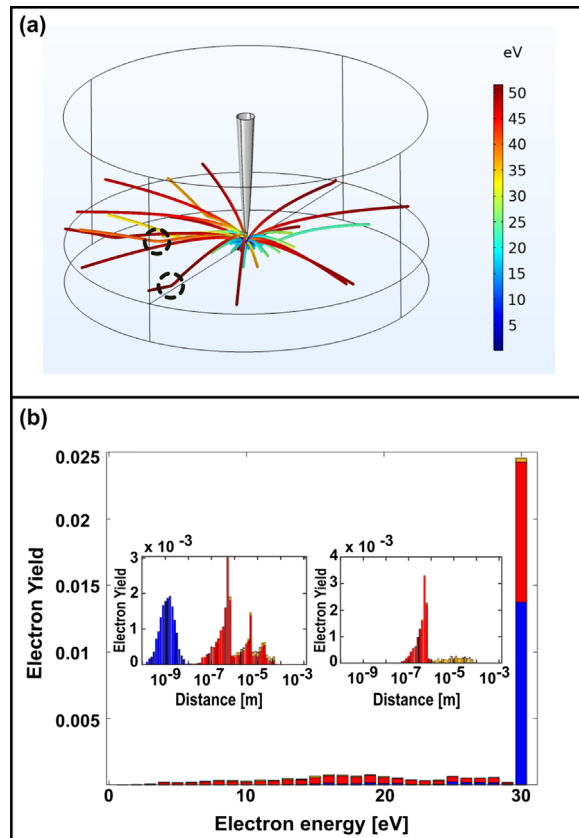


**FIG. 1.** (a) Initial trajectories of ejected electrons in the field emission regime. The electrons are started from the primary site indicated by the tip (gray) with different initial energies (color code given in the vertical bar). Their trajectory is displayed within a circle with 800 nm diameter. All electrons are deflected by the electric field in the tip-target region toward the surface. Some are reflected by the surface barrier (see, e.g., within the dotted circles). Those entering the surface scatter elastically and inelastically (not shown in the figure) with the constituents of the target (ion cores and electrons). (b) Spectrum of electrons reaching the detector, for a tip bias voltage of  $-30$  V. The blue bars represent electrons that were simulated in Geant4 only once (i.e., they emerged from the tip-sample junction and went on to strike the detector by skipping, without re-entering the material). The red (yellow) bars represent those electrons that were simulated twice (thrice) in Geant4 (i.e., a high energy electron has undergone one or more quantum reflections at the surface and then re-entered the material at some distance away from the tip-sample junction and then generated ejected electrons or undergone an elastic scattering event at that location). The inset on the left indicates the distance from the primary site of production of the electrons contributing to the elastic peak of the histogram (notice the horizontal logarithmic scale). The blue bars indicate that the electrons have passed through the Geant4 code only once and, therefore, originate from directly under the tip. The excitation of the remaining electrons extends up to the sample edge. For producing the inset on the right, quantum skipping was removed: all electrons from the primary site disappear from the elastic peak.

onto the surface (at distances—few tens of nm—from the primary site that depend on their energy), they can reenter the crystal [not shown in Fig. 1(a) for simplicity]. Alternatively, according to quantum mechanics,<sup>1</sup> there is a finite probability of being reflected back by the energy cliff at the interface between vacuum and surface. (In classical physics, particles are accelerated only forward at an energy cliff.) Some quantum reflection events are indicated by dotted circles in Fig. 1(a).

By virtue of the scattering events, some of the ejected electrons have the same kinetic energy as the primary ones when they arrive at the surface and are classified as the elastic electrons. Those with lesser kinetic energy (including the secondary<sup>17</sup> electrons) build the inelastic channel. Figure 1(b) shows a typical example of the spectral distribution of the electrons arriving at the detector. The bar colored in blue represents those electrons for which the Geant4 code was called only once, i.e., that emerged from the primary site and arrived at the detector by quantum skipping. As observed in the spectral distribution, they have the property of accumulating in the elastic channel. The bars colored in red/yellow are those electrons that emerge from the surface after the second/third run of the Geant4 code. They are seen to populate the entire spectral range. The inset on the left shows where the electrons used to create the spectral distribution were actually generated. The electrons colored in “blue” originate at the primary site, with the remaining ones building up a two-dimensional cascade<sup>15</sup> that extends up to the edge of the sample. For constructing the inset on the right, instead, quantum reflection was switched off: the electrons generated at the primary site disappear, only the two-dimensional cascade persists: quantum reflection is the essential mechanism for observing electrons emerging at the primary site.

Those electrons that reenter the target instead of skipping away are problematic for using the near-tip field emission mode as a lensless scanning electron microscope. In fact, they might excite further electrons away from the primary generation site. This produces a cascade-like process<sup>23</sup> that inexorably widens the spatial extension of the excitation. Recent model simulations<sup>15</sup> found that such a two dimensional cascade can reach mm distances from the junction. A scenario entailing cascade electrons could compromise both the spatial resolution and locality of the signal when the junction is run as ejected electron imaging electron microscope.<sup>23</sup> Yet, ejected electron imaging in this situation found a lateral spatial resolution of about one nanometer<sup>14</sup> and a subnanometer vertical resolution.<sup>14</sup> Moreover, in an experiment detecting the spin of the ejected electrons, juxtaposed magnetic domains of reversed magnetization could be resolved.<sup>23</sup> Accordingly, any experimental evidence about the true nature of the putative two-dimensional cascade is missing so far.

In the second part of this Letter, we have sought experimental evidence for the quantum skipping scenario. This entailed expanding the original instrument for spin polarization analysis (see Ref. 23) to include an energy filtering insertion device called a “Bessel box analyzer”<sup>27</sup> (short: BBx, see the [supplementary material](#)). The experiments use patterned samples fabricated by inserting a suitably designed mask between the source of the Fe-atoms and the (110)-surface of a W single crystal, casting shadows with geometry at will.<sup>23</sup> During deposition, the substrate is at room temperature. The observation that has actually triggered this work uses a mask containing a slit that produced an Fe stripe, a few 100  $\mu\text{m}$  wide, and two to three atomic layers (ALs) thick [sketched in Fig. 2(a)]. The lower and upper Fe-W boundary of the stripe is imaged by STM (Fig. 3). In the top section of image, Fig. 3(a),

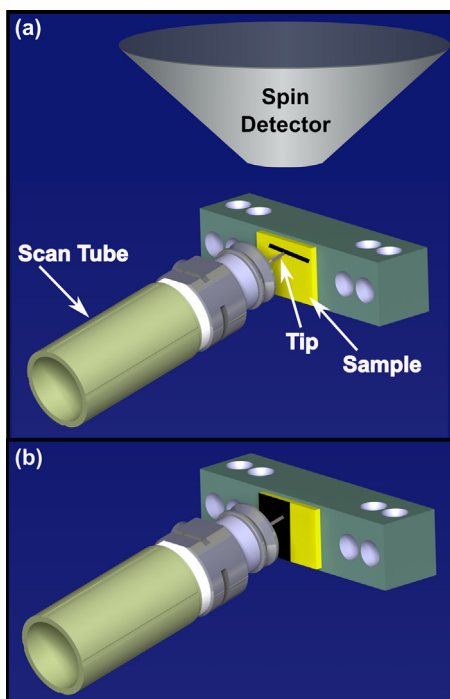


**FIG. 2.** (a) Sketch of the sample used for obtaining the data in Figs. 3(a)–3(c). [The entrance of the spin detector is also sketched on top of (a).] The horizontal dark line is the Fe stripe. The data in Figs. 3(a)–3(c) refer to the lower Fe-W boundary. The data in Fig. 3(d) refer to the upper boundary. (b) Sketch of the half-mask sample used for the data in Figs. 4(b)–4(d). The dark side is covered with Fe.

one recognizes an  $\approx 2$  AL thick Fe film from its typical morphology:<sup>14</sup> Fe atoms belonging to the second atomic layer appear as dense set of patches [brighter in Fig. 3(a)] on top of a continuous background (the first Fe layer). Also visible in Fig. 3(a) are the W(110) monatomic steps, running almost horizontally, separating the terraces on which the Fe film resides. After STM imaging, we retract the tip to the field emission regime<sup>14</sup> and measure the in-plane magnetization component of the surface as a function of the in-plane applied magnetic field  $B$  by detecting the corresponding component (designated by  $P$ ) of the spin polarization vector of the ejected electrons.<sup>23</sup> The data in Fig. 3 are taken at room temperature and without the use of the energy filtering device. The approximate horizontal position of the tip during the taking of the  $P$ – $B$  hysteresis curve is marked in the STM image. The “rectangular” hysteresis curve observed at the top location is typical of an Fe film with an in-plane ferromagnetic order. Moving down in Fig. 3(a), one proceeds away from the lower Fe-W boundary and the film becomes gradually thinner. The non-abrupt ending of the Fe film is a consequence of the penumbra resulting from the use of a mask, but is a welcome property: It allows tracing the vanishing of the ferromagnetic order with the decrease in film thickness. For example, the lowest hysteresis curve in Fig. 3(a) is measured on top of a Fe film with a thickness of only 1 AL. Proceeding further down in the image [Figs. 3(b) and 3(c)], the tip moves on top of regions with submonolayer thick Fe films. [In the bottom region of Fig. 3(c), the Fe film reduces to Fe dots with a density corresponding to about 0.1 AL.] Yet, the shape of the  $P$ – $B$  curve is still typical of ferromagnetic order,

although  $P$  has reduced by about a factor of 2. We call this finite  $P$  a “ghost” spin polarization: The onset of ferromagnetic order at room temperature for thin films of Fe on W(110) (deposited at room temperature) is at about 1.7 AL,<sup>28</sup> i.e., well above the thickness of the film in Fig. 3(c). The results for the upper Fe-W boundary are shown in Fig. 3(d). The spin polarization on top of the about 1.5 AL thick film (central circle) is already reduced by a factor of two with respect to the amplitude on a 2.5 AL thick film (lower circle). At the onset of the first AL (top circle), the spin polarization is almost vanishing.

The origin of this ghost polarization remained puzzling until the simulations presented in Fig. 1 opened a new degree of freedom—the skipping electrons, not interacting with the constituents of the target and, thus, potentially restoring the locality of the ejected electron imaging in the scanning field emission mode. The simulations induced us to seek the vanishing of this ghost spin polarization on a nominally non-magnetic surface by filtering out the inelastic component of the ejected electron spectrum with the insertion device. Figure 4 summarizes the results of the experiments performed without and with the insertion device. Figure 4(a) shows the evolution of the spin polarization as a function of the distance from the lower Fe-W boundary in the horizontal Fe stripe geometry of Fig. 2(a). The profiles were obtained in experiments similar to those of Fig. 3 [notice that the data of Figs. 3 and 4(a) were obtained within different experimental runs, so that their spin polarization is difficult to compare]. Relevant and meaningful is the relative change in spin polarization within the same experimental run). No energy filtering is applied in the experiments leading to the data of Fig. 4(a). At the Fe-W boundary, one observes a sharp drop of  $P$ , to a level, which is persistently non-vanishing on top of the non-ferromagnetic side. A similar behavior emerges in the profiles at the back of Fig. 4(b). They were obtained for the “half-mask” sample sketched in Fig. 2(b). The profile labeled with “none” is taken without energy selection, i.e., with no insertion device. The one labeled “BBx rear 0 V” is taken with the insertion device, but the rear voltage is such that almost no elastic electron is allowed to enter the spin detector. Both profiles show the ghost spin polarization observed in Fig. 4(a). Next we have two profiles with the rear BBx voltage adjusted to let only the elastic ejected electrons enter the spin detector. The boundary in the  $P$  vs distance profile appears as sharp as in the previous profiles, but the ghost spin polarization on top of W has almost vanished. [The small signal remaining—see, e.g., Ref. 29 for a hysteresis curve on nominally clean W—is probably due to the filtering not being entirely sharp and/or the presence of electrons in the elastic channel that are not originating from the primary site, see the red component in Fig. 1(b).] Finally, the insertion device is removed but the energy filtering is still performed, using some suitable settings for the electron optical lenses used within the spin detector itself. Again, only the elastic electrons are admitted into the spin detector and the ghost spin polarization vanishes. Figures 4(c) and 4(d) summarize the profiles at different primary energies, without (4c) and with (4d) energy filtering. Both boundaries appear similarly sharp in both profiles, but the ghost spin polarization recorded in (4c) vanishes in (4d). The energy filtering has produced the sought for locality of the signal in the ejected electron imaging mode of scanning field emission microscopy. Interestingly, the boundary in the energy-unfiltered mode is as sharp as the boundary in the energy-filtered mode. This can be understood as the primary site spin polarization of the ejected electrons being certainly larger on the Fe side than on the W side of the

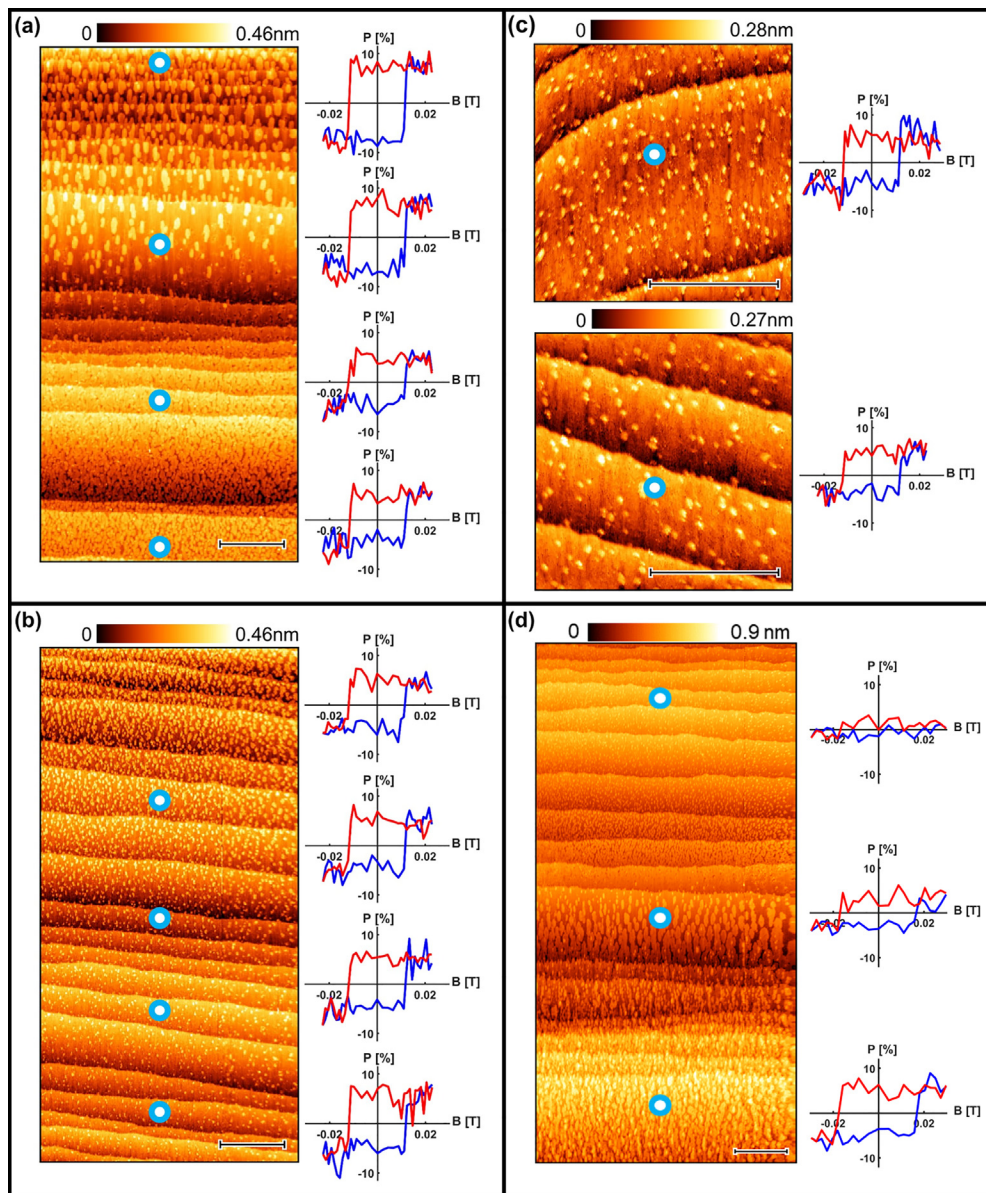


**FIG. 3.** STM images and ferromagnetic response at the lower and upper boundaries between the Fe stripe and W [see Fig. 2(a) for the description of the geometry]. The stripe is about  $425 \mu\text{m}$  wide. Experiments are performed at room temperature. The color code used to encode the tip displacement is given in the horizontal bars. STM is performed at constant current mode, i.e., during the scan, the tip displaces vertically to keep the tunneling current constant. The vertical displacement is, thus, a direct measure of the surface topography. (a)–(c) (Lower boundary), the film thickness decreases when moving down the image. (a) ( $200 \times 500 \text{ nm}^2$ ). On the top of the image, the film is about 2 AL thick. The rectangular hysteresis curves are measured with tip bias voltage of about  $-60 \text{ V}$ , field emitted currents of about  $150 \text{ nA}$ , and tip-target distance of about  $40 \text{ nm}$ . They are taken at the locations indicated in the STM image. (b) ( $200 \times 500 \text{ nm}^2$ ). Ferromagnetic order continues at sites where the Fe film has submonolayer thickness [bottom of (b)]. (c) ( $100 \times 100 \text{ nm}^2$ ). The center of the top image is about  $1.2 \mu\text{m}$  away from the center of (a). Fe atoms are build sparse dots. The film is about 0.15 AL thick. The hysteresis curve shows ferromagnetic order, albeit P has reduced by about a factor of 2 with respect to the top hysteresis in (a). In the bottom image of (c) [the center of which is about  $3.2 \mu\text{m}$  away from center of (a)], the film is only 0.12 AL thick but ferromagnetic order is still visible. (d) ( $250 \times 500 \text{ nm}^2$ ), bias voltage:  $\approx -46 \text{ V}$ . Current:  $60 \text{ nA}$ , tip-target distance:  $40 \text{ nm}$ .

boundary and the two-dimensional cascading process being unable to completely wipe out this initial difference.

The use of the unfiltered version of this technology to image a distribution of magnetic domains and the role of the cascading process

were discussed in Ref. 23. More recently,<sup>30</sup> we have found that the filtering of the elastic electrons produces a sizeable enhancement of the spin polarization contrast (i.e., the change in spin polarization) when going from one domain to an adjacent one.

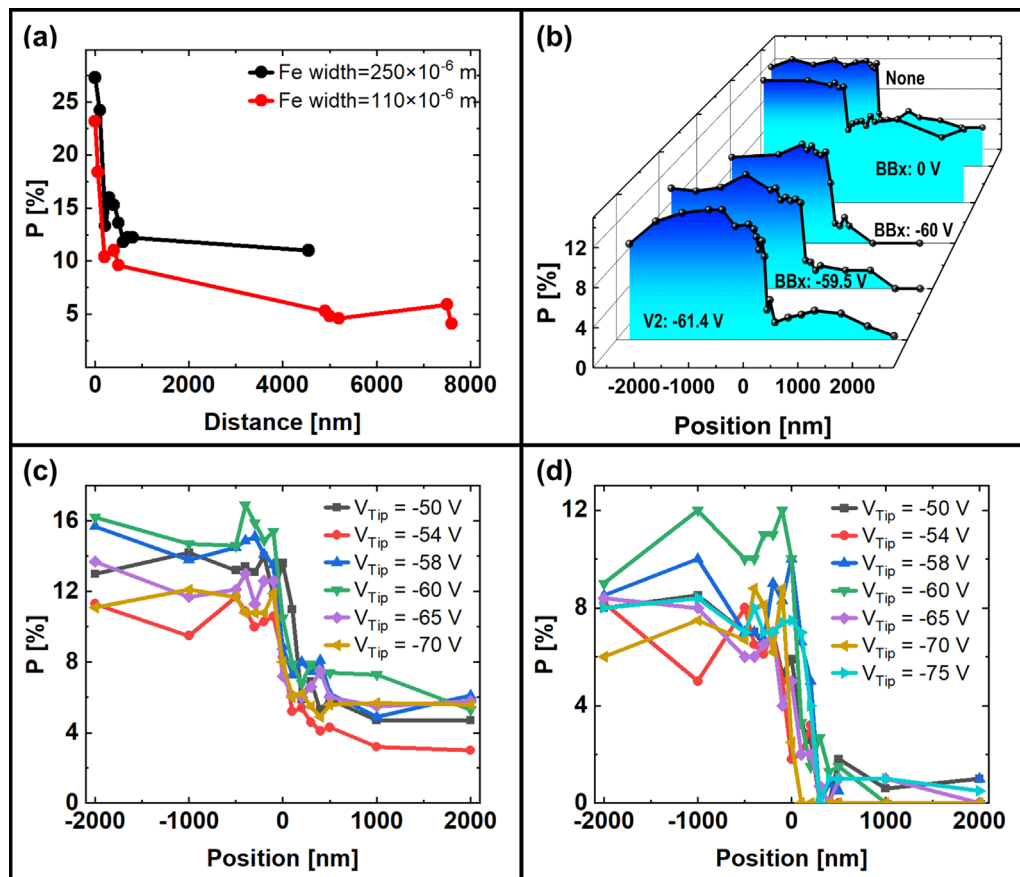


**FIG. 4.** (a) Summary of  $P$  vs distance from a Fe-W lower boundary [sample as in Fig. 2(a)]. Indicated is the width of the Fe stripe. (b)  $P$  profiles vs position in the vicinity of a Fe-W boundary (the origin of the horizontal axis). The sample is as in Fig. 2(b). The energy selection state is indicated in the profiles and is discussed in the text. Typically, for the hysteresis curves in (b) (BBx or V2 filtered), the voltage applied to the tip was  $-60$  V, the emission current about  $300$  nA and the tip sample distance was between  $100$  and  $150$  nm. The count rate achieved at the backscattering channels of the spin detector in the filtered mode was about  $15$  to  $40$  kHz, compared with the count rate of about  $200$  kHz in the unfiltered mode (which is the same order of magnitude as the one observed in the more conventional scanning electron microscopy with polarization analysis (SEMPA) method of magnetic imaging<sup>23</sup>). The displayed data amount to an average over ten loops. (c) Summary of  $P$  profiles for different tip bias voltages  $V_{\text{Tip}}$ , without energy filtering. The sample is as in Fig. 2(b). (d) Summary of  $P$  profiles for different tip bias voltages  $V_{\text{Tip}}$ , with energy filtering. The sample is as in Fig. 2(b).

See the [supplementary material](#) for detail of the simulations and of the experiments.

The authors would like to acknowledge COMSOL Multiphysics Support for all their considerable assistance in the simulation aspect of this work. The ISG group at ETH Zurich provided help (in particular Gürkan Myczko) in setting up the Geant4 package.

#### AUTHOR DECLARATIONS

##### Conflict of Interest

The authors declare that they have no competing financial interest.

##### Author Contributions

A.-K.T., J.W., and U.R. built the instrument and took the experimental data in Figs. 4(b)–4(d). J.Z. and U.R. took the data in Figs. 3 and 4(a). C.W. did the simulations. H.C. provided help with COMSOL. M.D., A.P., S.T., M.El-G., A.S. provided help with the

implementation of the BBx technology at ETH Zurich. C.W. and D.P. wrote the paper.

#### DATA AVAILABILITY

The data that support the findings of this study are available within the article and its [supplementary material](#).

#### REFERENCES

- <sup>1</sup>L. Nordheim, "Zur Theorie der thermischen Emission und der Reflexion von Elektronen an Metallen," *Z. Phys.* **46**, 833–855 (1928).
- <sup>2</sup>R. Niedermayer and J. Hölzl, "Reflexion sehr langsamer Elektronen an Metalloberflächen," *Phys. Status Solidi B* **11**, 651–656 (1965).
- <sup>3</sup>R. Cimino, I. R. Collins, M. A. Furman, M. Pivi, F. Ruggiero, G. Rumolo, and F. Zimmermann, "Can low-energy electrons affect high-energy physics accelerators?," *Phys. Rev. Lett.* **93**, 014801 (2004).
- <sup>4</sup>C. I. Vaz, C. Liu, J. P. Campbell, J. T. Ryan, R. G. Southwick III, D. Gundlach, A. S. Oates, R. Huang, and K. P. Cheung, "Observation of strong reflection of electron waves exiting a ballistic channel at low energy," *AIP Adv.* **6**, 065212 (2016).

- <sup>5</sup>X. Ying, J. P. Lu, J. J. Heremans, M. B. Santos, M. Shayegan, S. A. Lyon, M. Littman, P. Gross, and H. Rabitz, "Quantum reflection and transmission of ballistic two-dimensional electrons by a potential barrier," *Appl. Phys. Lett.* **65**, 1154–1156 (1994).
- <sup>6</sup>C. Angrick, J. Braun, H. Ebert, and M. Donath, "Spin-dependent electron reflection at W(110)," *J. Phys.* **33**, 115001 (2020).
- <sup>7</sup>J. Penfold and R. K. Thomas, "The application of the specular reflection of neutrons to the study of surfaces and interfaces," *J. Phys.* **2**, 1369–1412 (1990).
- <sup>8</sup>F. Shimizu, "Specular reflection of very slow metastable neon atoms from a solid surface," *Phys. Rev. Lett.* **86**, 987–990 (2001).
- <sup>9</sup>T. A. Pasquini, M. Saba, G.-B. Jo, Y. Shin, W. Ketterle, and D. E. Pritchard, "Low velocity quantum reflection of Bose-Einstein condensates," *Phys. Rev. Lett.* **97**, 093201 (2006).
- <sup>10</sup>Y. S. Ang, L. Caol, and K. Ang Lay, "Physics of electron emission and injection in two-dimensional materials: Theory and simulation," *InfoMat* **3**, 502–535 (2021).
- <sup>11</sup>Z. Zhang, Z. Peng, Z. Ma, and C. Zhang, "Effect of quantum reflection over the barrier on thermionic refrigeration," *J. Appl. Phys.* **128**, 044301 (2020).
- <sup>12</sup>R. Young, J. Ward, and F. Scire, "The topografiner: An instrument for measuring surface microtopography," *Rev. Sci. Instrum.* **43**, 999–1011 (1972).
- <sup>13</sup>F. Festy, K. Svensson, P. Laitenberger, and R. E. Palmer, "Imaging surfaces with reflected electrons from a field emission scanning tunnelling microscope: Image contrast mechanisms," *J. Phys. D* **34**, 1849–1852 (2001).
- <sup>14</sup>D. A. Zanin, L. G. De Pietro, Q. Peter, A. Kostanyan, H. Cabrera, A. Vindigni, T. Bähler, D. Pescia, and U. Ramsperger, "Thirty percent contrast in secondary-electron imaging by scanning field-emission microscopy," *Proc. R. Soc. A* **472**, 20160475 (2016).
- <sup>15</sup>W. S. M. Werner, M. Oral, T. Radlicka, J. Zelinka, I. Müllerova, A. Bellissimo, G. Bertolini, H. Cabrera, and O. Gürlü, "Scanning tunneling microscopy in the field-emission regime: Formation of a two dimensional electron cascade," *Appl. Phys. Lett.* **115**, 251604 (2019).
- <sup>16</sup>Y. Zhu, H. Inada, K. Nakamura, and J. Wall, "Imaging single atoms using secondary electrons with an aberration-corrected electron microscope," *Nat. Mater.* **8**, 808–812 (2009).
- <sup>17</sup>D. C. Joy, "Scanning electron microscopy: Second best no more," *Nat. Mater.* **8**, 776–777 (2009).
- <sup>18</sup>L. P. Muray, "Developments in low-voltage microscopy instrumentation," *Scanning* **33**, 155–161 (2011).
- <sup>19</sup>M. M. El-Gomati and C. G. H. Walker, "Toward quantitative scanning electron microscopy," in *Advances in Imaging and Electron Physics*, edited by P. W. Hawkes (Elsevier, 2014), Vol. 183, pp. 1–40.
- <sup>20</sup>E. Bauer, "Surface microscopy with low energy electrons: LEEM," *J. Electron Spectrosc. Relat. Phenom.* **241**, 146806 (2020).
- <sup>21</sup>I. Müllerova and L. Frank, "Scanning low-energy electron microscopy," *Adv. Imaging Electron Phys.* **128**, 309–443 (2003).
- <sup>22</sup>K. Bian, C. Gerber, A. J. Heinrich, D. J. Müller, S. Scheuring, and Y. Jiang, "Scanning probe microscopy," *Nat. Rev. Methods Primers* **1**, 36 (2021).
- <sup>23</sup>U. Ramsperger and D. Pescia, "Vectorial, non-destructive magnetic imaging with scanning tunneling microscopy in the field emission regime," *Appl. Phys. Lett.* **115**, 112402 (2019).
- <sup>24</sup>S. Agostinelli *et al.*, "GEANT4: A simulation toolkit," *Nucl. Instrum. Methods Phys. Res., Sect. A* **506**, 250–303 (2003).
- <sup>25</sup>E. Kieft and E. Bosch, "Refinement of Monte Carlo simulations of electron-specimen interaction in low-voltage SEM," *J. Phys. D* **41**, 215310 (2008).
- <sup>26</sup>See [www.comsol.com](http://www.comsol.com) for "COMSOL Multiphysics™ Version 5.5, COMSOL AB, Stockholm, Sweden."
- <sup>27</sup>A. Suri, A. Pratt, S. Tear, C. Walker, and M. El-Gomati, "Next generation secondary electron detector with energy analysis capability for SEM," *J. Microsc.* **279**, 207–211 (2020).
- <sup>28</sup>H. J. Elmers, J. Hauschild, H. Höche, and U. Gradmann, "Magnetism of Fe(110)on W(110): Finite width scaling of stripes and percolation between islands," *Phys. Rev. Lett.* **73**, 898–901 (1994).
- <sup>29</sup>L. De Pietro, G. Bertolini, Q. Peter *et al.*, "Spin-polarised electrons in a one-magnet-only Mott spin junction," *Sci. Rep.* **7**, 13237 (2017).
- <sup>30</sup>A.-K. Thamm, "Energy and spin resolved scanning field emission microscopy and a new instrument for low temperature imaging," Report ETH No. 28082 (2021).